

Evaluation of Hydrodynamic Performance of A Marine Train Advancing in Waves

Feng-Shen Zhu^a, Zhi-Ming Yuan^a, De-Feng Wu^b, De-Qing Zhang^{a,c *}

^a Department of Naval Architecture, Ocean & Marine Engineering, University of Strathclyde, Glasgow, G4 0LZ, UK

^b School of Marine Engineering, Jimei University, Xiamen, 361021, PR China

^c College of Engineering, Ocean University of China, Qingdao, 266100, PR China

Abstract:

Marine trains, configured by multiple vessels advancing in a row, provide a promising solution for reducing fuel consumption and enhancing transport efficiency in the maritime industry. As a brand-new concept for marine transportation, there remains a notable gap concerning its hydrodynamic performance. The hydrodynamic interactions and mechanical connections cause their dynamic behaviors to differ significantly from those of traditional vessels. This study aims to investigate the hydrodynamic responses of marine trains composed of multiple carriages under different connection types, providing valuable insights for the design of this joint system to promote its engineering applications. First, an in-house code based on a two-step numerical approach was developed to conduct their hydrodynamic responses, initially solving the hydrodynamic interaction problem, followed by mechanical coupling using the constraint matrix method. The accuracy of this in-house code was thoroughly validated against the published experimental and numerical results. Then, the responses of a marine train configuration with two moving ships were analyzed to examine the effects of various connection types. The results showed that when two ships are either hinged or rigidly connected, the motion response amplitude operators (RAOs) are significantly reduced compared to those of free ships; however, both connection types experience substantial vertical shear forces at the joints. In contrast, the sliding-hinged connection presents a viable solution for marine trains, as it does not increase motion responses while significantly reducing vertical shear forces. Moreover, the responses of a marine train configuration with five moving ships with sliding-hinged connections were analyzed to investigate the effect of advancing speed, joint position, and the gap between ships. The motion RAOs of the vessels increased significantly with rising advancing speed, while remaining relatively insensitive to variations in joint position and the gap between ships.

Keywords: Marine train; multiple advancing vessels; hydrodynamic interactions; mechanical connection; motion response

1. Introduction

As global trade continues to expand, the demand for maritime transportation rises steadily. Consequently, reducing logistics costs and enhancing transport efficiency have become critical challenges for the shipping industry. One promising solution to address these challenges is the concept of the "marine train". This innovative system involves multiple vessels traveling in tandem to create a long, parallel mid-body, reducing wave-making resistance and lowering fuel consumption (DPRPA, 2020). The findings of Yuan et al. (2021) offer compelling support for this concept, demonstrating how ducklings swimming in single-file formation reduce wave resistance and even generate propulsion through wave-riding and wave-passing. Building on this, Zhu and Yuan (2024) demonstrated that ships arranged in similar formations can also harness these hydrodynamic benefits, resulting in greater fuel efficiency and reduced emissions. Beyond its environmental and economic advantages, the marine train also offers significant operational flexibility. Individual vessels in the formation can be detached and sent to ports with limited infrastructure, where larger ships might be unable to dock. Furthermore, because each vessel operates autonomously, the system does not require all units to wait for the loading and unloading of others. This independence allows for more efficient port operations and quicker turnarounds, optimizing both operational costs and scheduling.

Within the marine train concept, two primary approaches are typically utilized. The first involves directly linking multiple consecutive vessels using physical connectors, ensuring stable and coordinated transit operations. The second approach utilizes compressive forces, facilitated by a specially designed hull form, to keep the vessels aligned and connected without the need for physical connectors. A notable example is the Seasnake concept (Anderson, 2013), where a tractor unit pulls multiple barge modules connected by a ball-and-socket coupling. The Articulated Tug Barge (ATB) system (Brown and Runyon, 2022), however, uses a tugboat to push load-carrying barges, with articulated connectors securing the tug within a notch in the barge. The U.S. Navy's Improved Navy Lighterage System (INLS) (Guha et al., 2013) employs small warping tugs to propel barges connected by a bull-nose and socket arrangement, with a flexor tension member that allows each unit to pitch relative to the others. However, large forces that can develop between units pose challenges for mechanical connections. In response, the U.S. Navy's Transoceanic Connectorless Seatrain Concept

(Karafiath et al., 2009) features sharp bows that fit into V-shaped notches in the sterns of adjacent units, relying on compressive forces to maintain connection. Each unit is equipped with water jets at the transom, positioned on either side of the notch, to assist with alignment and control during transit. Despite the advantages of this system, it poses challenges in designing bumpers and fenders to effectively manage the forces and prevent damage during transit. Figure 1 illustrates one marine train concept, in which the "engine ship" provides the propulsion force for the entire assembly, and the barges are connected through mechanical connections.

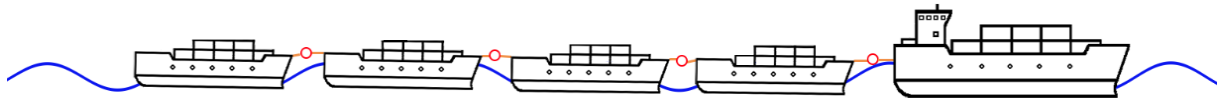


Figure 1. A marine train configuration with five ships.

Resistance reduction, turning performance, shear forces at joints, and motion response are key considerations in the design of marine trains. Mizine and Karafiath (2015) designed a high-speed trimaran sea train with a ball-and-opening socket arrangement between units. Their model tests demonstrated that a four-unit sea train reduced resistance per unit by 24% to 30% within the 10 to 30-knot speed range. Additionally, they found that the maximum turning diameter of the assembled sea train was approximately three times the total length of the system. Zhang et al. (2021) tested an articulated pusher-barge system and found that both the ATB system and pusher experienced significant increases in sinkage at higher speeds and shallow drafts. To further investigate the vertical forces on the coupling of a pusher tug-barge system in waves, Mumford (1993) developed a numerically fast three-dimensional solution method to consider the interactions between the two hulls in coupled modes of motion at zero speed, based on the unified slender body theory. Miller et al. (2001) conducted integrated tug-barge (ITB) model tests and found that the maximum longitudinal, transverse, and vertical connection forces occur at wave encounter angles of 0° , 45° , and 225° , respectively. Qin et al. (2023) used STAR-CCM+ to investigate a conceptual sea train featuring a small water-plane-area trimaran in heading wave. They compared two configurations: one with physical connections that allowed relative pitch motion between vessels, and another with non-physical connections. Their results revealed that the drag reduction between the two configurations was minimal, while the physically connected system significantly reduced the pitch motion of each vessel.

The motion responses of marine trains in waves are complex, resulting from hydrodynamic interactions between vessels as well as the dynamic coupling of interconnected components. Accurate prediction of these hydrodynamic responses is crucial for ensuring the safety and efficiency of marine train operations, as vessel interactions can amplify motion responses and potentially damage mechanical connections. To date, much research has focused on the hydrodynamic interactions of interconnected floating structures. Gao et al. (2011) investigated the effect of the placement and rotational stiffness of flexible line connections on the hydroelastic response of very large floating structures (VLFS). Their findings indicated that hinge-line connectors, when optimally positioned, are more effective than rigid connectors in minimizing both hydroelastic responses and stress resultants. Ren et al. (2019) explored the impact of various outermost connector designs on the hydrodynamic performance of modular multi-purpose floating structures (MMFS). Their results showed that the hydrodynamic responses of the MMFS system are influenced by connector type, wave phase, and wavelength. Additionally, the hinge-type connector design is found to play a key role in reducing bending moments and shear forces on connectors under extreme marine conditions. Bispo et al. (2022) developed a numerical model to study wave interactions with a moored articulated VLFS, finding that the rotational stiffness of the hinges significantly influenced both the vertical displacement of the structure and the mooring line tensions. Zhang et al. (2023) analyzed the motion behavior of large arrays formed by multiple floaters connected by hinges, observing that while hinge constraints significantly suppressed heave motion, they also induced strong pitch motion across a broader range of wavelengths. Li et al. (2023) conducted a hydroelastic and expansibility analysis of a Modular Floating Structure (MFS) with multi-directional hinge connections. Their findings highlighted that greater stiffness results in a more pronounced structural response, with the system's reactions intensifying as stiffness increases. Additionally, they observed that smaller module sizes cause larger vertical displacements and reduced moments, while the hydroelastic behavior remains largely unaffected by module size in long-wave conditions.

Although significant work has been done to understand the motion responses of interconnected floating structures, there remain few studies that systematically investigate the dynamic responses of marine trains in waves. This research gap results in a lack of scientific support for the engineering

design of such structures. This paper explores the hydrodynamic interactions of marine trains with various physical configurations using an in-house code MHydro (Yuan et al., 2015). A three-dimensional Boundary Element Method (BEM) is employed to calculate wave-induced forces and hydrodynamic coefficients, while the constrained matrix method models the connections between vessels. The in-house code is validated through typical cases, including a single ship advancing in head sea and two interconnected barges in waves. Additionally, the motion response amplitude operators (RAOs) of a marine train with two ships are analyzed, considering both non-physical connections and different connection styles. Finally, the effects of advancing speed, joint positions, and the gap between ships on the motion responses of a marine train configuration comprising five ships are investigated.

2. Mathematical formulations

2.1 Velocity potential

An in-house code MHydro is employed to investigate ships advancing in a single-file formation in regular waves. As shown in Figure 2, two sets of right-handed coordinate systems are adopted: the global coordinate system $O-XYZ$ fixed to the earth and local coordinate systems $o_n - x_n y_n z_n$ ($n = 0, 1, 2, \dots, N$) fixed to each ship. In the global coordinate system, the plane $z = 0$ represents the undisturbed free surface, with the z -axis pointing upward and the y -axis directed to the starboard. The incident wave angle β is defined as the angle between the wave propagation direction and the ship's velocity U . Specifically, $\beta = 90^\circ$, 135° and 180° correspond to beam, oblique and head seas, respectively.

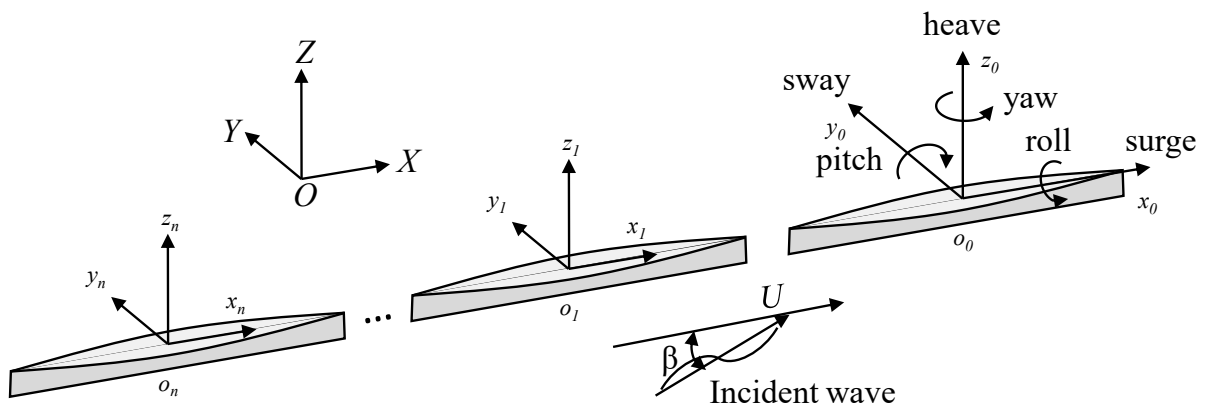


Figure 2. Coordinate systems of multiple moving ships.

Assuming the fluid is incompressible, inviscid, and the flow is irrotational, the fluid domain can be described by a velocity potential φ satisfying Laplace equation,

$$\frac{\partial^2 \varphi}{\partial x^2} + \frac{\partial^2 \varphi}{\partial y^2} + \frac{\partial^2 \varphi}{\partial z^2} = 0 \quad (1)$$

For a fleet of ships with forward speed U in waves, the wave-induced motions and loads are computed using linear diffraction and radiation theory. The total velocity potential in the flow field can be decomposed into

$$\varphi_T(x, y, z, t) = \varphi_b + \varphi_u e^{-i\omega_e t} \quad (2)$$

On the right-hand side, the sum of the first term represents the steady flow potential due to the base flow, while the second term denotes the wave velocity potential. The base-flow potential φ_b is expressed as

$$\varphi_b = -Ux + \varphi'_b(x, y, z), \quad (3)$$

where the Neumann-Kelvin model (Doctors and Beck, 1987) is applied, assuming the base flow to be an undisturbed uniform flow. Consequently, the steady flow velocity is $\varphi_b = -Ux$, with $\varphi'_b = 0$.

The wave velocity potential is given by

$$\varphi_u = \varphi_0 + \varphi_7 + \sum_{j=1}^6 -i\omega_e \eta_j \varphi_j \quad (4)$$

where φ_0 , φ_7 and φ_j is the spatial velocity potentials of the incident wave, diffracted wave, and radiated wave, respectively and η_j represents the complex motion amplitude in the j -th mode ($j = 1, 2, \dots, 6$ represent surge, sway, heave, roll, pitch, and yaw mode of motions, respectively). The incident velocity potential is expressed by

$$\varphi_0 = -\frac{ig\eta_0 \cosh k(z+h)}{\omega_0 \cosh kd} e^{i[k(x\cos\beta + y\sin\beta)]} \quad (5)$$

where ω_0 is the incident wave frequency and η_0 is the incident wave magnitude. The encounter wave frequency can be obtained by

$$\omega_e = \omega_0 - Uk\cos\beta \quad (6)$$

In present study, the shallow water effect is not considered. If the water depth h is given, the wave number k can be determined using the dispersion relation

$$\frac{\omega_0^2}{g} = k \tanh kh \quad (7)$$

2.2 Boundary conditions

The entire computational domain consists of body surfaces, free surface, control surface, and the seabed. The corresponding boundary conditions are imposed as follows:

On the free surface, i.e., $z = 0$,

$$g \frac{\partial \varphi_j}{\partial z} - \omega_e^2 \varphi_j + 2i\omega_e U \frac{\partial \varphi_j}{\partial x} + U^2 \frac{\partial^2 \varphi_j}{\partial x^2} = 0 \quad (8)$$

On the seabed, i.e., $z = -h$,

$$\frac{\partial \varphi}{\partial n} = 0 \quad (9)$$

For radiation wave velocity, on the oscillating ship surface,

$$\frac{\partial \varphi_j^n}{\partial n} = -i\omega_e n_j + U m_j; \quad \text{for } j = 1, \dots, 6 \quad (10)$$

where the generalized normal n_j is defined by

$$n_j = \begin{cases} n, & \text{if } i = 1, 2, 3 \\ n \times r, & \text{if } i = 4, 5, 6 \end{cases} \quad (11)$$

Here, n represents the outward unit normal vector and r represents the position vector with respect to the origin of the coordinate system. The m -term m_j considers the effect of the steady flow on the radiation boundary condition, which can be simplified to

$$\begin{aligned} (m_1, m_2, m_3) &= (0, 0, 0) \\ (m_4, m_5, m_6) &= (0, n_3, -n_2) \end{aligned} \quad (12)$$

On the other fixed ship surface,

$$\frac{\partial \varphi_j^n}{\partial n} = 0; \quad \text{for } j = 1, \dots, 6 \quad (13)$$

For the diffraction velocity, on all ship surfaces,

$$\frac{\partial \varphi_7^n}{\partial n} = -\frac{\partial \varphi_0^n}{\partial n}; \quad \text{for } j = 7 \quad (14)$$

2.3 Numerical implementation

The entire computational boundary is composed of free-, control-, body- surface and seabed, which is discretized into a number of quadrilateral panels with constant source density $\sigma(q)$. The velocity potential at the field point $q(x, y, z)$ induced by the source point $p(x_0, y_0, z_0)$ can be

expressed as

$$\varphi(p) = \iint_S \sigma(q)G(p, q)dS_q, \quad (15)$$

where $G(p, q)$ denotes the Rankine-type Green function. The mirror image method is employed to account for the seabed boundary condition, given by

$$G(p, q) = \frac{1}{r} + \frac{1}{r'}, \quad (16)$$

where

$$\begin{cases} r = \sqrt{(x - x_0)^2 + (y - y_0)^2 + (z - z_0)^2} \\ r' = \sqrt{(x - x_0)^2 + (y - y_0)^2 + (z + z_0 + 2h)^2} \end{cases}. \quad (17)$$

Thus, the discretization of the computational boundary can be simplified to include only the free surface, control surface, and body surface, as shown in Figure 3. The body surface S_b , free surface S_f , and control surface S_c are divided into N_b , N_f and N_c panels, respectively, resulting in a total of N panels in the discretized boundary. Consequently, the velocity potential at any source point p_i can be expressed as

$$\varphi(p_i) = \sum_{j=1}^N \sigma_j \iint_{S_b+S_f+S_c} G(p_i, q)dS_q = \sum_{j=1}^N \sigma_j G_{i,j}, i = 1, 2, \dots, N. \quad (18)$$

The differential terms of velocity potential in different directions then can be written as

$$\frac{\partial \varphi}{\partial x}(p_i) = 2\pi\sigma_i + \sum_{\substack{j=1, \\ j \neq i}}^N \sigma_j \iint_{S_b+S_f+S_c} \frac{\partial}{\partial x_i} G(p_i, q)dS_q = 2\pi\sigma_i + \sum_{\substack{j=1, \\ j \neq i}}^N \sigma_j G_{i,j}^x, i = 1, 2, \dots, N, \quad (19)$$

$$\frac{\partial \varphi}{\partial z}(p_i) = 2\pi\sigma_i + \sum_{\substack{j=1, \\ j \neq i}}^N \sigma_j \iint_{S_b+S_f+S_c} \frac{\partial}{\partial z_i} G(p_i, q)dS_q = 2\pi\sigma_i + \sum_{\substack{j=1, \\ j \neq i}}^N \sigma_j G_{i,j}^z, i = 1, 2, \dots, N, \quad (20)$$

$$\frac{\partial \varphi}{\partial n}(p_i) = 2\pi\sigma_i + \sum_{\substack{j=1, \\ j \neq i}}^N \sigma_j \iint_{S_b+S_f+S_c} \frac{\partial}{\partial n_i} G(p_i, q)dS_q = 2\pi\sigma_i + \sum_{\substack{j=1, \\ j \neq i}}^N \sigma_j G_{i,j}^n, i = 1, 2, \dots, N. \quad (21)$$

The analytical solutions for the influence coefficient $G_{i,j}$ and its differential terms in different directions $G_{i,j}^x$, $G_{i,j}^z$ and $G_{i,j}^n$ are provided by Hess and Smith (1964), while detailed numerical

implementation routines can be found in Yuan et al. (2015). By applying equations (18-21) to the boundary conditions of the body, free, and control surfaces, an equation system for the source density σ_j can be established as follows:

$$[P_{i,j}]\{\sigma_j\} = [Q_i], i = 1,2, \dots, N; j = 1,2, \dots, N. \quad (22)$$

where $P_{i,j}$ represents the coefficient matrix and Q_i the matrix comprising the boundary conditions for each panel. Once σ_j is determined, the potential and velocity component at any point within the computational domain can be calculated using equations (18-21).

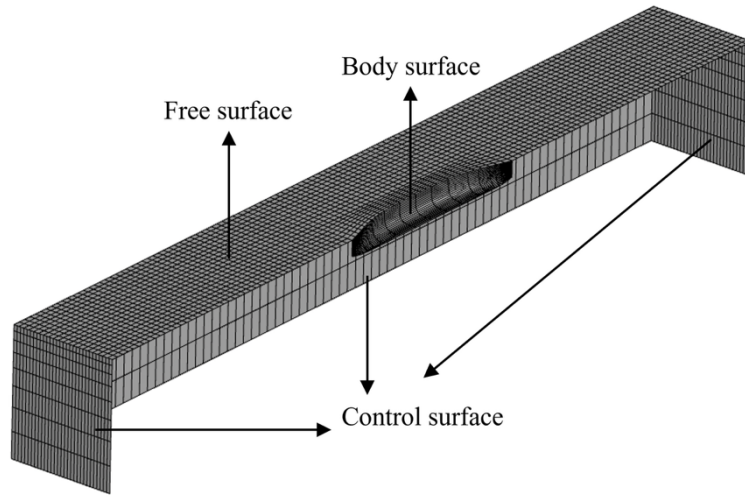


Figure 3. Computational domain and panel distribution of a single ship model.

2.4 Hydrodynamic forces and motion equations

Once the diffraction and radiation velocity potential are solved, the pressure on the body surface can be obtained based on Bernoulli's equation,

$$P_j = -\rho\eta_j(i\omega_e\varphi_j + U\frac{\partial\varphi_j}{\partial x}). \quad (23)$$

The radiation forces or moments in i -th mode of the m -th ship due to j -th mode of the n -th ship can be calculated by

$$F_{ij}^{mn} = \iint P_j n_i dS_m \quad (24)$$

From Equations (23) and (24), added mass coefficients μ_{ij} and potential damping coefficients λ_{ij} can be expressed as

$$\mu_{ij}^{mn} = -\frac{\rho}{\omega_e} \iint [Im(\varphi_j^n) - \frac{U}{\omega_e} \frac{\partial Re(\varphi_j^n)}{\partial x}] n_i dS_m \quad (25)$$

$$\lambda_{ij}^{mn} = -\frac{\rho}{\omega_e} \iint [Re(\varphi_j^n) - \frac{U}{\omega_e} \frac{\partial Im(\varphi_j^n)}{\partial x}] n_i dS_m \quad (26)$$

The wave excitation force in six degrees of freedom on n -th ship can be determined by integrating the pressure distributions of both the incident and diffracted waves over the wetted body surface,

$$F_i^n = \iint (P_0 + P_7) n_i ds, \quad i = 1, 2, \dots, 6 \quad (27)$$

According to Newton's second law, the motion components of n -th ship in the frequency domain can be obtained by

$$[-\omega_e^2 (M^n + \mu_{ij}^{mn}) + i\omega_e \lambda_{ij}^{mn} + K^n] \eta_i^n + \sum_{m=0, m \neq n}^N [(-\omega_e^2 \mu_{ij}^{mn} + i\omega_e \lambda_{ij}^{mn}) \eta_i^n] = F_i^n \quad (28)$$

where M and K represent the generalized mass matrix and restoring matrix. For convenience, the motion equation can be simplified as

$$A\eta = F \quad (29)$$

where A is the stiffness matrix and F is the external forces and moments on the system.

For multi-body constrained systems, the dynamic coupling due to different connections should be incorporated into the motion equations. A comprehensive discussion on the derivation of constrained dynamic systems is provided by Shabana (2009). According to Hamiltonian formalism (Vinogradov and Krasil'shchik, 1975), the constrained system can be expressed as

$$\Pi = \frac{1}{2} \eta^T A \eta - \eta^T F \quad (30)$$

Considering there are rigid constrains between some of the degrees of freedom, the constraint equation is given by

$$D\eta = 0 \quad (31)$$

By means of Lagrange multiplier γ , the function Π can be modified to

$$\Pi = \frac{1}{2} \eta^T A \eta - \eta^T F + \gamma^T D\eta \quad (32)$$

Combining Equations (19) and (23) and taking the variations with respect to η leads to

$$\begin{Bmatrix} [A]_{6n \times 6n} & [D^T]_{6n \times l} \\ [D]_{l \times 6n} & [0]_{l \times n} \end{Bmatrix} \begin{Bmatrix} [\eta]_{6n \times 1} \\ [\gamma]_{l \times 1} \end{Bmatrix} = \begin{Bmatrix} [F]_{6n \times 1} \\ [0]_{l \times 1} \end{Bmatrix} \quad (33)$$

where Lagrange multiplier γ represents the generalized force associated with the constraints in a system, D represents the constraint matrix, n and l denote the number of ships and total number of constraints at all joints.

Once the motion amplitudes in six degrees of freedom of each ship are determined, the wave elevation on the free surface can be calculated using the dynamic free surface boundary condition expressed as

$$\zeta = \sum_{n=0}^N \frac{1}{g} \left[\nabla(\varphi_s - Ux) \nabla(\eta_i^n \varphi_j^n + \eta_0^n \varphi_0^n + \eta_7^n \varphi_7^n) + i\omega_e(\eta_i^n \varphi_j^n + \eta_0^n \varphi_0^n + \eta_7^n \varphi_7^n) \right] = Re(\zeta) + Im(\zeta) \quad (34)$$

where η_7 represent the diffraction wave magnitude. The total wave magnitude can be calculated by

$$|\zeta| = \sqrt{Re(\zeta)^2 + Im(\zeta)^2} \quad (35)$$

3. Numerical validation

The method described above is incorporated into the in-house code MHydro to investigate the hydrodynamic performance of marine trains. The validations are established through two published case studies: two free-floating ships advancing in waves; two interconnected floating barges stationary in waves. The combination of these two validation cases encompasses the entire simulation process of marine trains, addressing wave actions, hydrodynamic interactions among multiple floating bodies, mechanical constraints of connectors, and the advancing speeds of the bodies.

3.1 Two floating ships with forward speed

The benchmark experiments of two different ships advancing in head seas are employed to validate present in-house code. The main dimensions of the tanker (Ship_a) and the LNG carrier (Ship_b) are provided in Table 1. Details of the model test setup can be found in Ronæss (2002). In the experimental test, Ship_a is restrained in surge and sway, while heave, roll, pitch, and yaw motions remain free. Ship_b is restrained in surge, sway, and yaw, with the remaining degrees of freedom unconstrained. The longitudinal centers of the two ships are staggered, with a transverse separation of 1.25 m and a longitudinal offset of 0.59 m. Both ships advance at the same forward speed of 0.608 m/s, corresponding to a Froude number of $F_r = U/\sqrt{gL_a} = 0.1$.

Table 1. Main dimensions of tanker and LNG ship.

Parameter	Tanker	LNG ship
Length between perpendicular	$L_a = 3.76m$	$L_b = 2.28m$
Breadth	$B_a = 0.625m$	$B_b = 0.387m$
Draught	$T_a = 0.232m$	$T_b = 0.124m$
Displacement	$V_a = 0.4355t$	$V_b = 0.074t$
Block coefficient	$C_B^a = 0.83$	$C_B^b = 0.68$
Water plane area coefficient	$C_w^a = 0.90$	$C_w^b = 0.79$
Longitudinal CoG (rel. midship)	$X_G^a = 0.086m$	$X_G^b = -0.01m$
Vertical CoG (rel. calm waterline)	$Z_G^a = -0.052m$	$Z_G^b = 0.012m$
Radius of inertia for roll	$r_{44}^a = 0.175m$	$r_{44}^b = 0.103m$
Radius of inertia for pitch	$r_{55}^a = 1.008m$	$r_{55}^b = 0.604m$
Radius of inertia for yaw	$r_{66}^a = 1.008m$	$r_{66}^b = 0.604m$

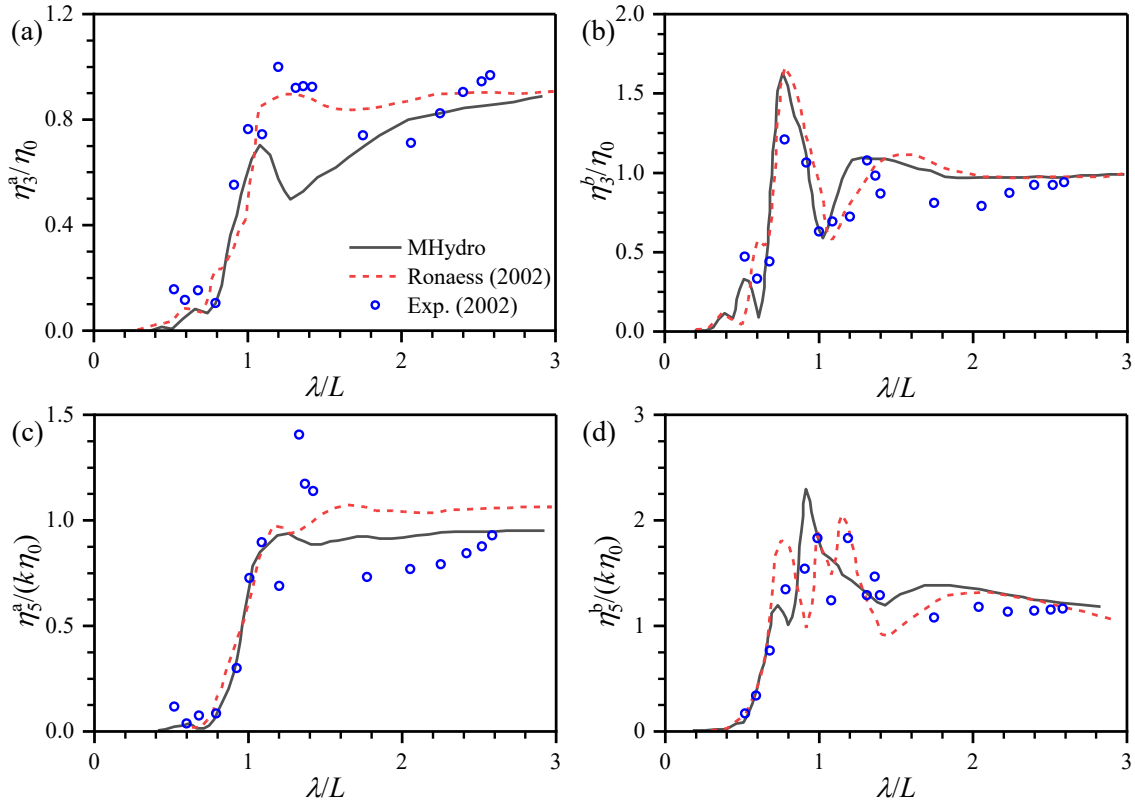


Figure 4. Response amplitude operators of two different ships advancing in head seas. (a) Heave of ship_a; (b) heave of Ship_b; (c) pitch of ship_a; (d) pitch of Ship_b.

Figure 4 compares the experimental results, the unified theory (Ronæss, 2002), and the present numerical predictions. The present results in heave and pitch motion of both ships generally have a satisfactory agreement with those of experimental data. However, notable discrepancies are observed in Figure 4(a) and 4(c) at $\lambda/L_a = 1.2$ and $\lambda/L_a = 1.3$, corresponding to the resonant frequencies of heave and pitch for Ship_a, respectively. In contrast, the numerical simulations predict resonance at approximately $\lambda/L_a = 1$ for both heave and pitch motions of Ship_a. This deviation is attributed to

the trim suspension in the model test setup (Ronæss, 2002). Overall, this validation case shows that the present in-house code can accurately predict the hydrodynamic interactions between multiple floating bodies advancing in waves and their motion responses.

3.2 Floating bodies with mechanical connection

Figure 5 (a) and (b) illustrate the vertical and rotational motions at the hinge point when two same barges are connected by a hinge in head sea. The barges are modelled as cuboids, with their main dimensions listed in Table 2. Newman (1994) employed the mode expansion technique to solve this hinged multi-body problem, while Sun et al. (2011) utilized the constraint matrix to model the hinge connection. It can be observed that the results from MHydro show good agreement with the published data. A significant difference between the two methods is observed: the constraint matrix method predicts a small peak in both heave and pitch motions at $\lambda/L = 1.125$, corresponding to the combined length of one barge and half the gap. In contrast, no such peak is observed using the mode expansion method.

Table 2. Main dimensions of two interconnected barges.

Parameter	Value
Length, L (m)	40
Breadth, B (m)	10
Draught, T (m)	5
Displacement, V (m ³)	2000
Gap between barges (m)	10
Water depth (m)	$+\infty$

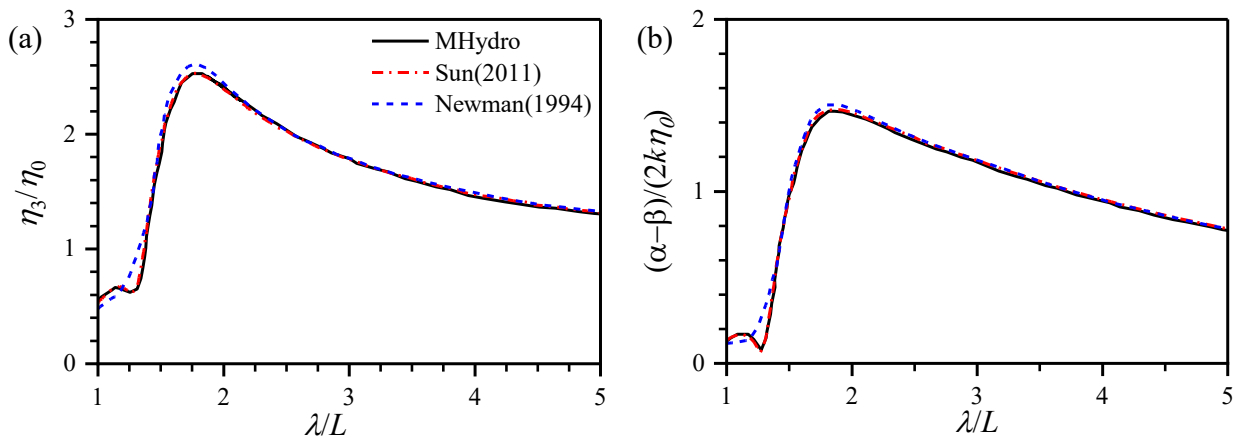


Figure 5. Motions of two hinged barges. (a) Vertical motion at the hinge; (b) rotation of the hinge. Here, $(\alpha - \beta)$ is the relative rotation between the two barges.

Figure 6 (a) illustrates the heave motion of rigidly connected barges, with the results once again indicating a satisfactory agreement. Figure 6 (b) shows the vertical shear force for both the hinged and rigid connections, which are identical. The vertical shear forces at the connection point between the barges consist of wave excitation forces, inertia forces, and hydrodynamic radiation forces. The wave excitation forces are the same for both connections. The remaining forces can be categorized into symmetric and anti-symmetric modes, with only the anti-symmetric modes contributing to the vertical force. However, the vertical force remains unchanged regardless of whether the connection is rigid or hinged. Overall, this validation case shows that the present in-house code can accurately predict the hydrodynamic interactions between multiple floating bodies under the wave actions and mechanical constraints of connectors.

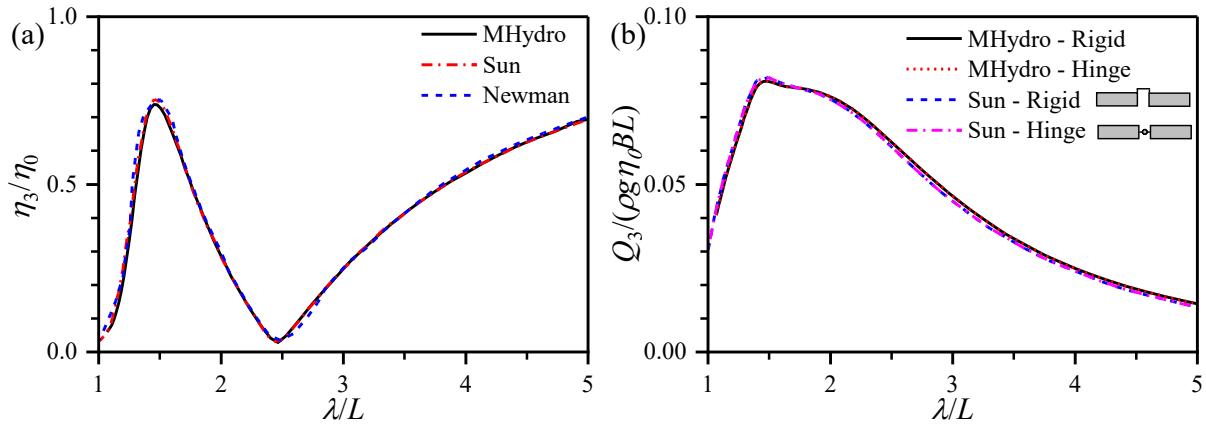


Figure 6. Non-dimensionalized heave motion of barges and vertical shear force of connectors. (a) Heave motion of rigidly connected barges; (b) vertical shear forces at hinged and rigid joints. Here, Q_3 is the actual value of the vertical shear force at joints.

4. A marine train configuration with two ships

4.1 Non-physical connection

A marine train configuration, comprising two ships without physical connection, is analyzed to investigate the differences in motion responses between ships operating within the train and those moving independently. Here, a blunt Wigley hull with a length-to-beam ratio (L/B) of 5:1 and a length-to-draft ratio (L/T) of 10:1 is adopted in the numerical calculation. The main dimensions of the blunt Wigley hull are presented in Table 3.

Table 3. Main dimensions of blunt Wigley hull

Parameter	Value
Length, L (m)	4
Breadth, B (m)	0.8
Draught, T (m)	0.4
Displacement, (m ³)	0.588
Center of rotation above base, KR (m)	0.4
Center of gravity above base, KG (m)	0.26
Radius of inertia for pitch, K_{yy} (m)	1

Figure 7 illustrates the non-dimensionalized heave and pitch motions for both a single ship and two ships in head sea, with a gap of $0.1L$ between the ships. The uppercase letters "L" and "T" in the upper corner represent the leading and trailing ships, respectively. As the forward speed increases, the differences in RAOs between the leading ship in a single-file formation and the single ship gradually diminish. It is clear that the RAOs of the leading ship are identical to those of the single ship at $F_r = 0.3$, as the trailing ship has minimal influence on the wave field of the leading ship at this speed. The Brard number ($\tau = U\omega_e/g$) is commonly used to compare the relationship between the ship's speed and the wave propagation speed it generates. At $\lambda/L = 0.5$, the Brard number equal to 2.16, while the Brard number is 0.48 at $\lambda/L = 4$. When the Brard number is greater than 0.25, the forward propagation velocity of the waves generated by the trailing ship is lower than the ship's advancing speed. This is further supported by Figures 8 and 9, which show the added mass and potential damping for the leading ship due to its own motion (L-L), for the trailing ship due to its own motion (T-T), for the leading ship affected by the trailing ship (L-T), and for the trailing ship affected by the leading ship (T-L). It can be found that the added mass and potential damping of the leading ship induced by the motion of the trailing ship are nearly zero. However, since the trailing ship is in the wake of the leading ship, its RAOs are significantly influenced by the leading ship. Notably, the peaks for the heave and pitch motions of the trailing ship are significantly higher than those of the leading ship when resonance occurs at $\lambda/L = 1.7$, due to wave superposition.

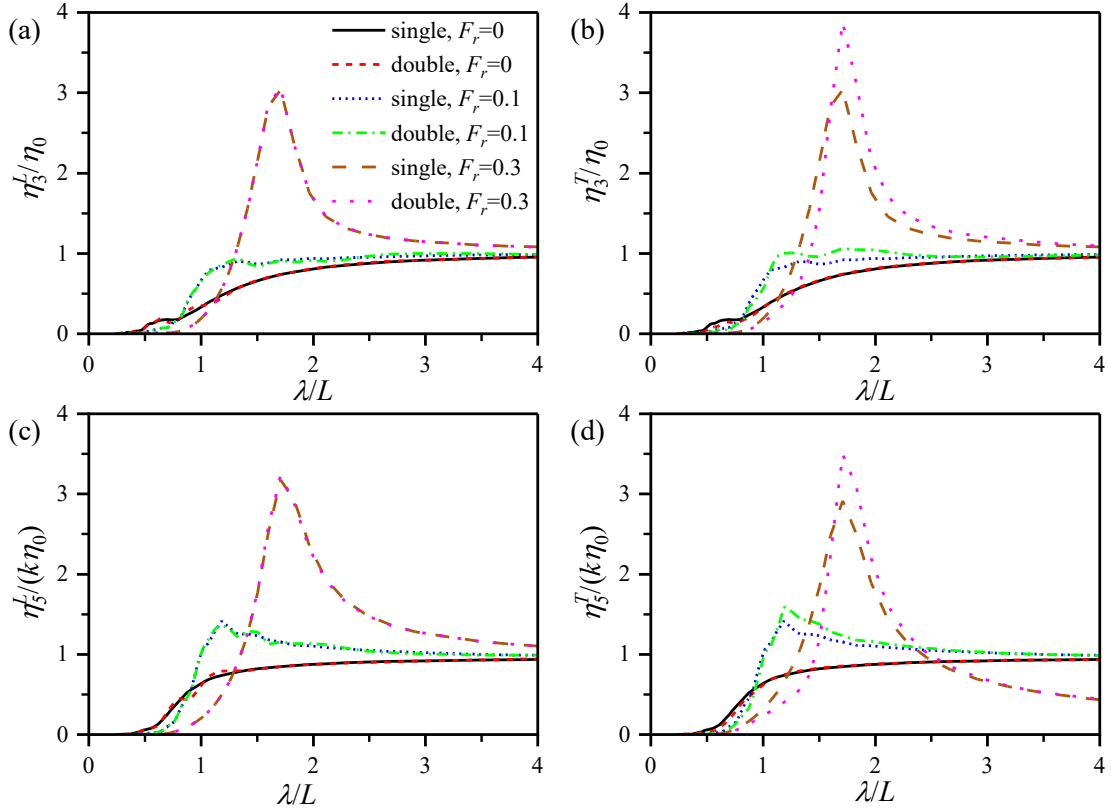


Figure 7. Comparison of RAOs for a single ship and two ships moving in a head sea at different speeds F_r . Heave: (a) leading ship; (b) trailing ship. Pitch: (c) leading ship; (d) trailing ship. In the legend, "single" refers to the results of a single moving ship, while "double" denotes the results of two ships moving in a single-file formation.

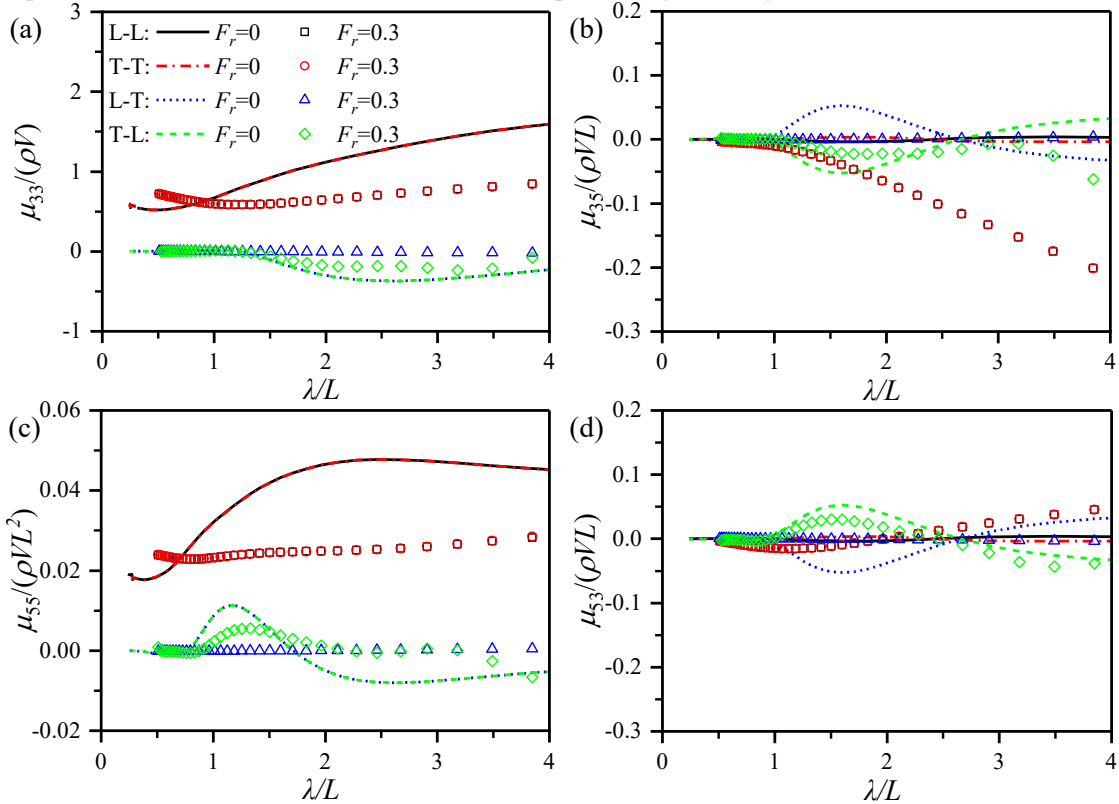


Figure 8. Added mass of two ships moving in a head sea at different speeds F_r . (a) Heave-induced heave added mass; (b) pitch-induced heave added mass; (c) pitch-induced pitch added mass; (d) heave-induced pitch added mass. In the legend, L-L indicates the effect of the leading ship on itself, T-T indicates the effect of the trailing ship on itself, L-T indicates the effect of the trailing ship on the leading ship, and T-L indicates the effect of the leading ship on the trailing ship.

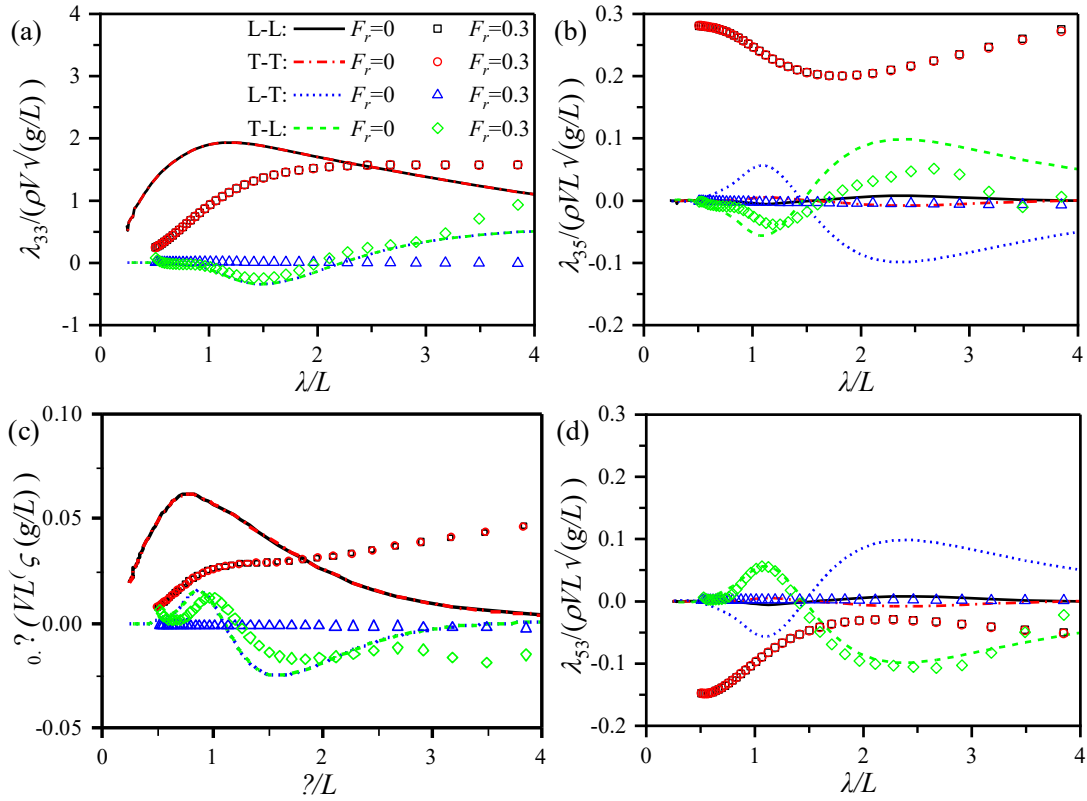


Figure 9. Potential damping of two ships moving in head sea at different speeds F_r . (a) Heave-induced heave damping; (b) pitch-induced heave damping; (c) pitch-induced pitch damping; (d) heave-induced pitch damping. In the legend, L-L indicates the effect of the leading ship on itself, T-T indicates the effect of the trailing ship on itself, L-T indicates the effect of the trailing ship on the leading ship, and T-L indicates the effect of the leading ship on the trailing ship.

In addition, the RAOs of both leading and trailing ships are nearly identical when the forward speed is zero, except when the λ/L ratio is less than 1, as shown in Figure 7. This similarity can be explained by examining both the hydrodynamic coefficients and the wave excitation forces. As illustrated in Figures 8 (a) and (c) and 9 (a) and (c), the hydrodynamic coefficients for two stationary ships are identical for heave-induced heave and pitch-induced pitch added mass and potential damping. In Figures 8 (b) and (d) and 9 (b) and (d), the coefficients for self-induced pitch-heave and heave-pitch added mass and potential damping are nearly zero, while these coefficients induced by the other ship are equal in magnitude but opposite in sign. Therefore, the hydrodynamic coefficients do not account for the observed differences. Instead, these discrepancies primarily arise from variations in the wave excitation forces acting on the two ships. As shown in Figure 10, the wave excitation force on the leading ship exhibits oscillations when the λ/L ratio is less than 1, corresponding to the oscillations observed in its heave and pitch motions at these ratios. Although the wave excitation forces and moments are higher for the leading ship compared to the trailing ship when the λ/L ratio exceeds 3,

there is no notable difference in the motion responses of the two ships. Both ships exhibit similar RAOs close to 1, as they move in sync with the incident waves.

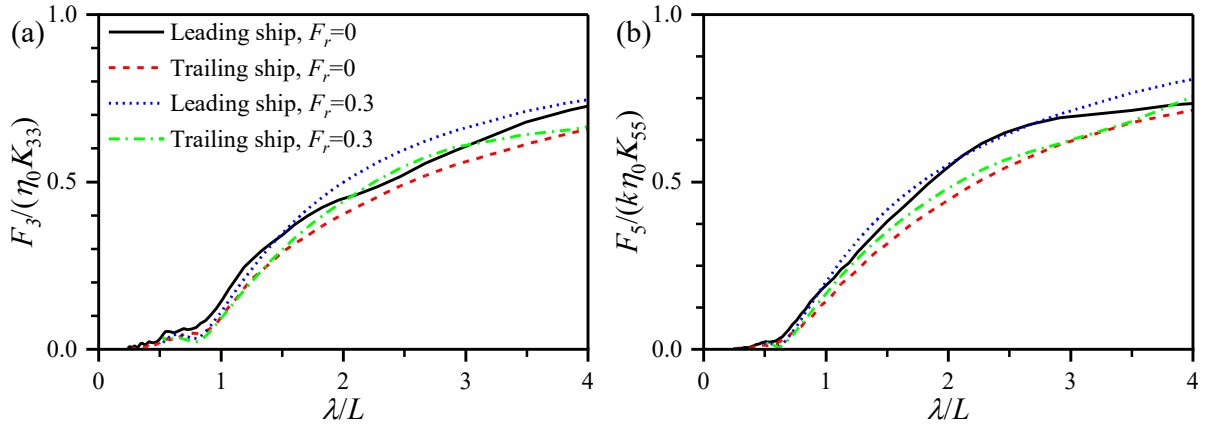


Figure 10. Wave excitation forces. (a) Heave force; (b) pitch moment.

Figure 11 illustrates the real part of the radiated wave patterns generated by the unit heave motion of two ships, both advancing and stationary, in a head sea with $\lambda/L = 1.83$. At $F_r = 0$, the wave patterns exhibit strong symmetry, demonstrating that the added mass and potential damping in heave, induced by the heave motion of the other ship, are identical for both vessels. This observation is consistent with the results shown in Figures 8 (a) and 9 (a). Additionally, at $F_r = 0.3$, the waves are convected downstream in a distinct V-shape distribution. Similarly, in the diffraction fields, the waves are also convected downstream, with the effect being significantly more pronounced at $F_r = 0.3$ compared to $F_r = 0$, as shown in Figure 12.

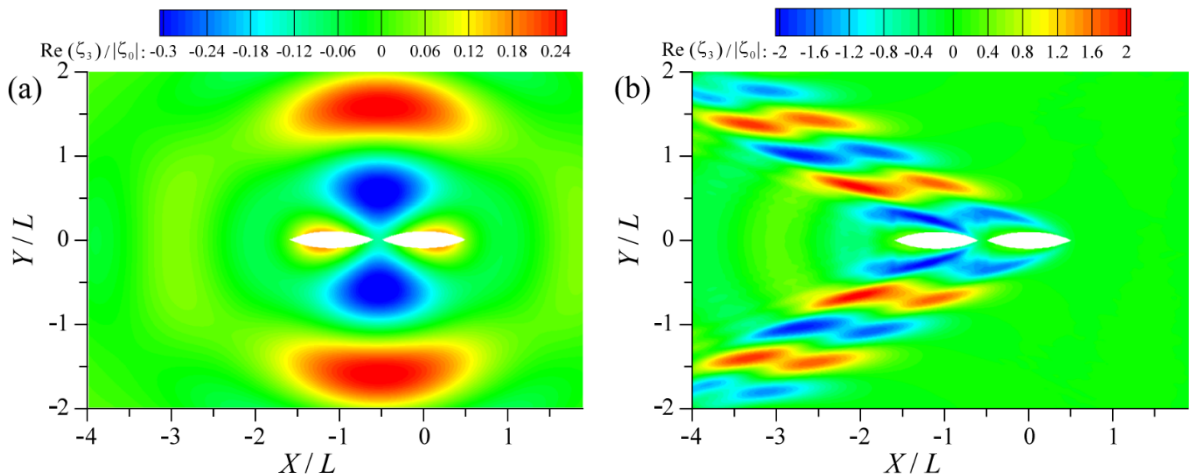


Figure 11. Real part of radiation wave pattern for unit heave motion at $\lambda/L = 1.83$. (a) $F_r = 0$; (b) $F_r = 0.3$.

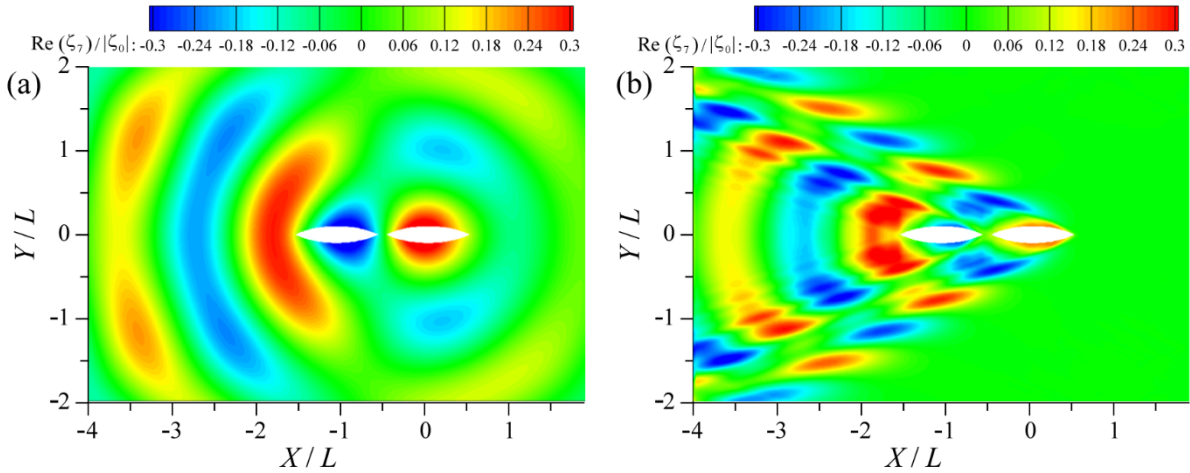


Figure 12. Real part of diffraction wave pattern at $\lambda/L = 1.83$. (a) $Fr = 0$; (b) $Fr = 0.3$.

4.2 Physical connection

Three types of mechanical connections are considered in the design of marine trains, as detailed in Table 4 and illustrated in Figure 13. A rigid connection fully constrains all six degrees of freedom between two ships, causing them to behave as a single, rigid body. A hinged connection allows relative pitch motion between the ships, while the other five degrees of freedom remain continuous at the hinge point. Finally, a sliding-hinged connection releases the heave, pitch, and yaw motions, enabling relative movement along these axes, while constraining the surge, sway, and roll motions at the joint, ensuring their continuity.

Table 4. Different mechanical connections.

Connections	Surge	Sway	Heave	Roll	Pitch	Yaw
Rigid	-	-	-	-	-	-
Hinged	-	-	-	-	✓	-
Sliding-hinged	-	-	✓	-	✓	✓

“✓” and “-” denote released and constrained states, respectively.

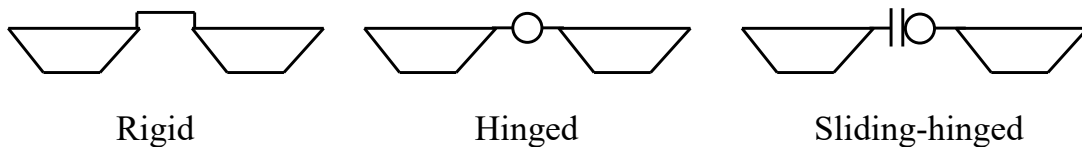


Figure 13. Different mechanical connection types.

Figure 14 illustrates the RAOs for different connections when two ships advance at $Fr = 0.3$ in head sea, with a gap of $0.1L$. The heave and pitch motions of the two ships with a rigid connection are

significantly smaller compared to those with hinged connection or sliding-hinged connections, and the RAOs of the leading ship are identical to those of trailing ship. In the case of a hinged connection, the heave and pitch motions of the leading ship are comparable to or slightly larger than those with a sliding-hinged connection, while the trailing ship's motions are significantly reduced with the hinged connection compared to the sliding-hinged connection. Additionally, resonance in the heave and pitch motions of the leading ship is observed around $\lambda/L = 1.7$ for both hinged and sliding-hinged connections, although the resonance magnitude are different. This indicates that the overall motion patterns are primarily governed by the wave loads acting on the ships, when mechanical connections are not considered, and that the variation in motions is influenced by the types of constraints.

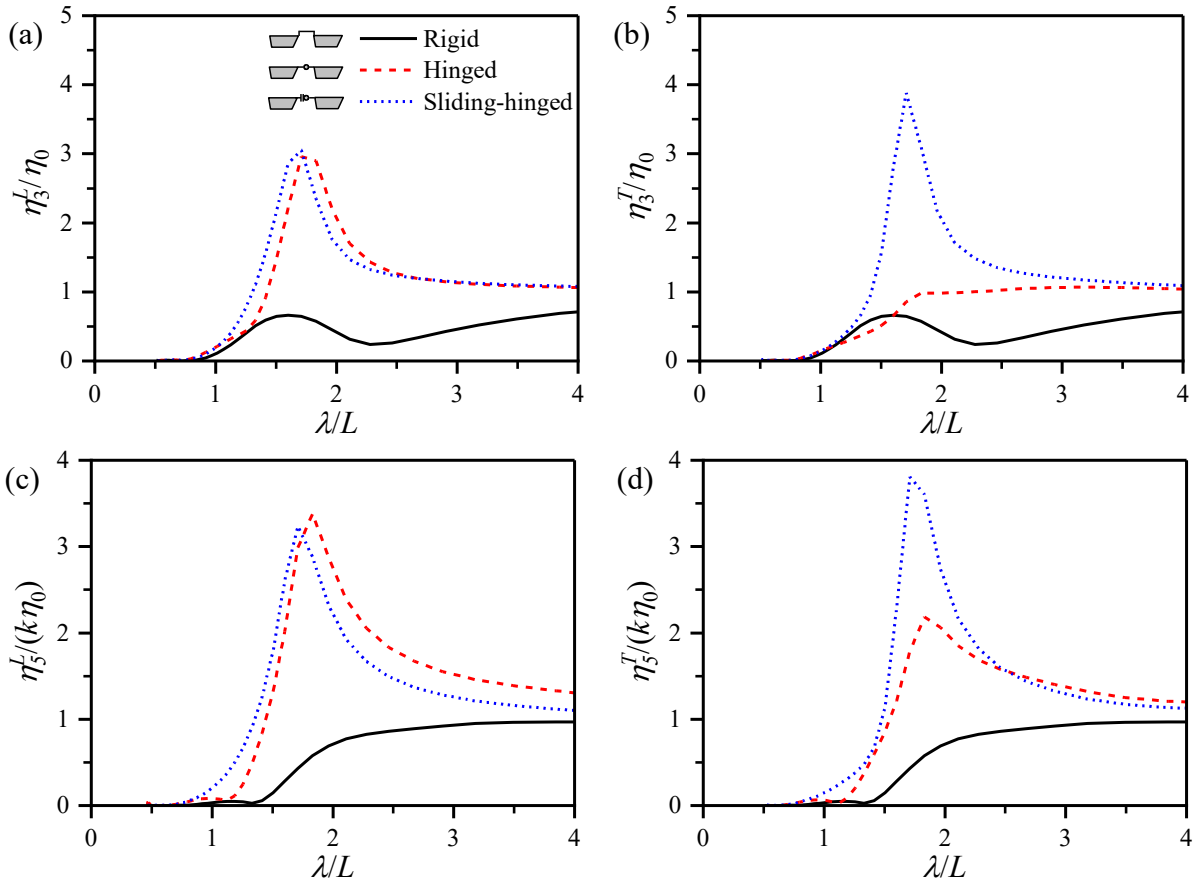


Figure 14. RAOs for different connections between two ships advancing at $F_r = 0.3$ in head sea. Heave: (a) leading ship; (b) trailing ship. Pitch: (c) leading ship; (d) trailing ship.

Figure 15 illustrates the vertical shear forces at the joints for both rigid and hinged connections at $F_r = 0$ and 0.3 , respectively. Similar to two hinged barges in waves, the vertical shear forces for both connection types are identical when two ships are stationary. The peaks of the vertical shear forces for both connection types at $F_r = 0.3$ are higher than those observed at zero speed, because the wave

excitation forces at $F_r = 0.3$ are generally higher than at $F_r = 0$. For the rigid connection at $F_r = 0.3$, a single peak in vertical shear force is observed, whereas the hinged connection shows two distinct peaks. The shared peak at $\lambda/L = 1.3$ for both connections is attributed to the phase difference in motion between the two ships in waves. The second peak, observed in the hinged connection at $\lambda/L = 1.7$, can be explained by the resonance in the motion response, as demonstrated in Figure 14. For this peak, the magnitude of motion is the dominant factor. It is important to note that the peaks of the vertical shear force reach up to half the weight of the ship itself, which could easily lead to damage of the mechanical connections, posing significant risks to their overall integrity.

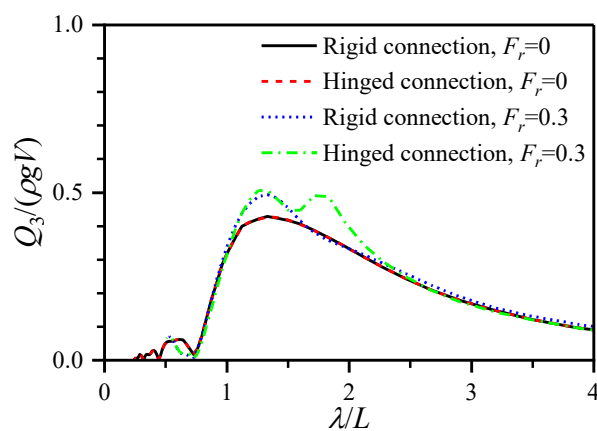


Figure 15. Vertical shear force at the joints for rigid and hinged connections.

Figure 16 (a) and (b) compare the RAOs for two ships with non-physical and sliding-hinged connections, both advancing at $F_r = 0.3$ in head seas with a $0.1 L$ gap between them. In these conditions, the heave and pitch motions of the ships with the sliding-hinged connection are identical to those observed with the non-physical connection. This is due to the coupling of surge, heave, and pitch motions under head sea conditions, with no interaction from the sway, roll, and yaw motions. The sliding-hinged connection effectively releases the constraints on heave and pitch between the two ships, resulting in a behavior similar to that of the non-physical connection. Figures 16 (c) to (e) compare the RAOs for the same ships with non-physical and sliding-hinged connections in oblique seas. In this case, the heave and pitch motions of both ships with the sliding-hinged connection remain identical to those with the non-physical connection. However, the roll motion differs, as the sliding-hinged connection does not release the roll constraint between the ships. Overall, the application of sliding hinges does not increase the motion response of the connected floating bodies, and the internal forces

within this type of connector are significantly lower than those associated with other types of connectors. This makes sliding hinges a suitable choice for the connection form of marine trains in practical engineering applications.

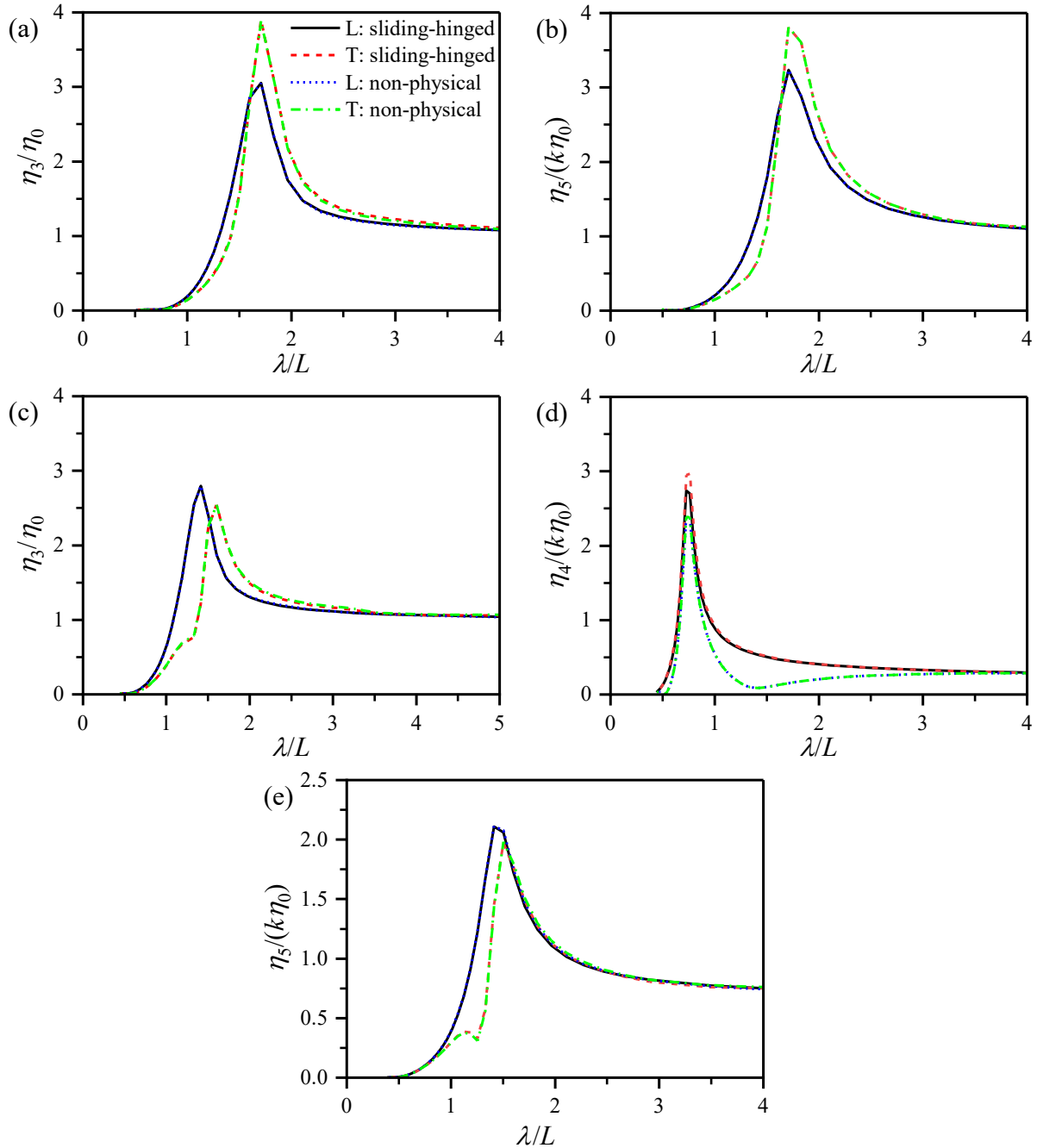


Figure 16. Comparison of RAOs between sliding-hinged and non-physical connections. Head sea: (a) Heave; (b) pitch. Oblique sea: (c) Heave; (d) roll. (e) pitch.

5. A marine train configuration with five ships

5.1 Effect of advancing speed

A marine train consisting of five ships connected by sliding-hinged joints is analyzed in head sea to investigate the effect of advancing speed. Figures 17 and 18 illustrate the RAOs for various advancing speeds with a gap of $0.1 L$. The results demonstrate a notable increase in RAOs as the advancing speed rises. Additionally, the resonance frequency progressively shifts towards longer wavelengths with moving speed increasing. This shift can be attributed to the Doppler effect: as the ship advances in head sea, the incident waves at the bow are compressed and effectively slow down, resulting in shorter wavelengths. As a result, the resonance condition is reached at longer wavelengths (lower wave frequency) as speed increases. Furthermore, with higher speed, more energy accumulates around the hull, leading to greater motion responses at resonance.

The RAOs of these ships show special patterns at a constant speed. For example, as shown in Figure 18 (c), when the wavelength is shorter than the resonance wavelength, pitch motion decreases from the leading ship to the last carriage. In contrast, when the wavelength exceeds the resonance wavelength, pitch motion increases. This behavior is attributed to the phase superposition of waves generated by these ships. For wavelengths shorter than the resonance wavelength, destructive interference occurs, leading to reduced RAOs along the convoy. Conversely, for longer wavelengths than the resonance wavelength, constructive interference dominates, resulting in increased RAOs. In general, to ensure the safety of marine trains during practical engineering operations, a maximum safe forward speed should be specified during the design state. Furthermore, by assessing whether the wavelength exceeds the resonance wavelength, it is possible to identify the positions of vessels within the array that experience maximum motion and require special attention to safety.

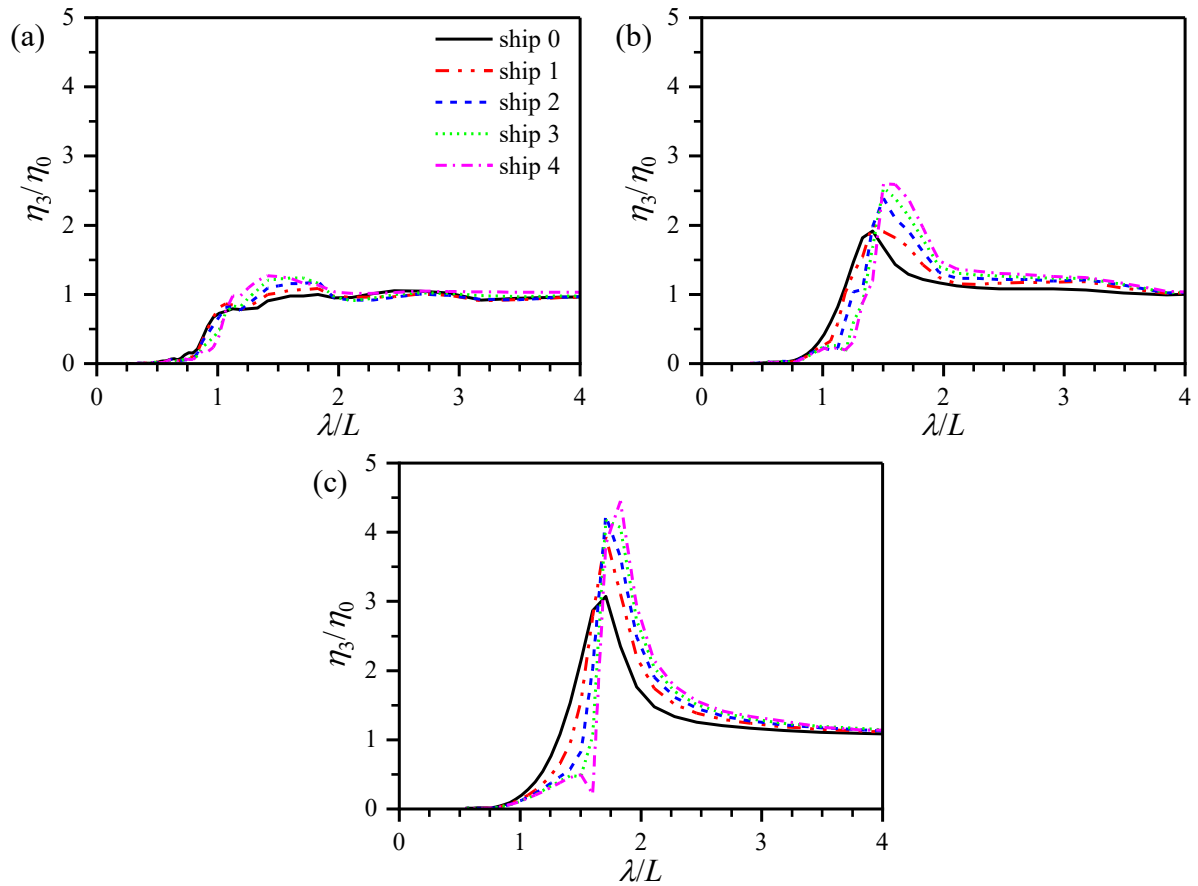


Figure 17. Heave motion at different speeds with a gap of $0.1 L$. (a) $F_r = 0.1$; (b) $F_r = 0.2$; (c) $F_r = 0.3$.

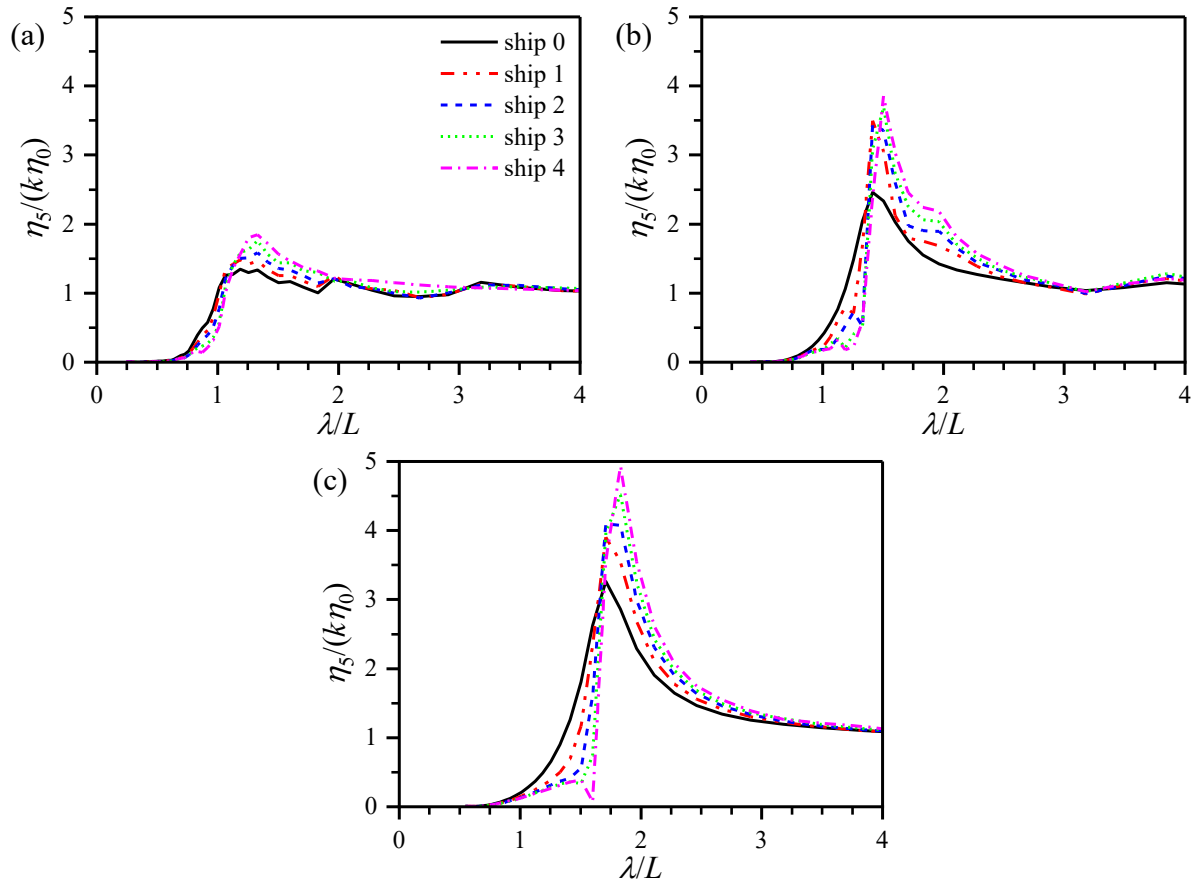


Figure 18. Pitch motion at different speeds with a gap of $0.1 L$. (a) $F_r = 0.1$; (b) $F_r = 0.2$; (c) $F_r = 0.3$.

Figure 19 illustrates the wave fields for different incident wavelengths at $F_r = 0.3$. The total wave magnitude around each ship effectively explains the RAOs observed for the corresponding vessel. For instance, at $\lambda/L = 1.6$, the wave magnitude around the engine ship is significantly higher than those around the carriages, resulting in greater heave and pitch motions for the engine ship compared to the carriages. At $\lambda/L = 1.83$, resonance occurs, progressively amplifying the motion responses along the marine train, with the last carriage experiencing the largest and most unexpected motion responses. Beyond the resonance wavelength, the wave magnitude quickly decreases as the incident wavelength increases. Therefore, to ensure operational safety, it is recommended to avoid resonance wavelengths at different speeds.

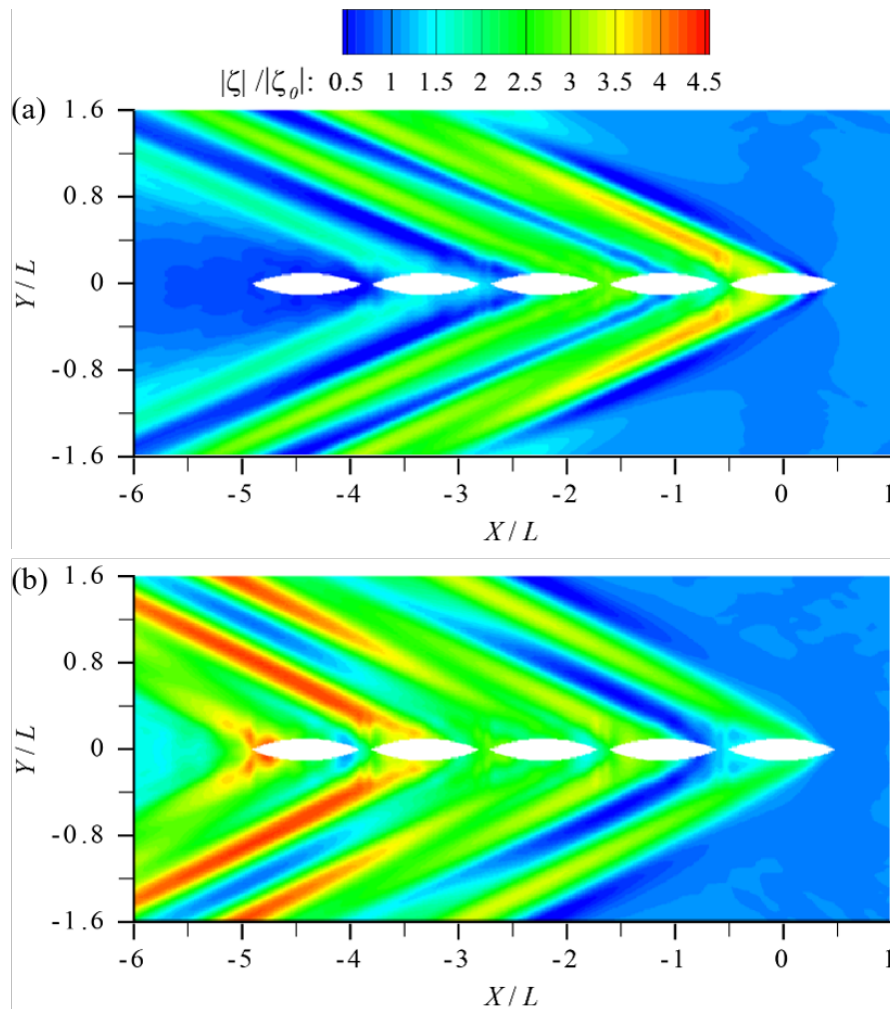


Figure 19. Wave magnitude for different wavelengths at $F_r = 0.3$: (a) $\lambda/L = 1.6$; (b) $\lambda/L = 1.83$.

5.2 Effect of installation position of joints

The installation positions of the joints are considered at three locations, all on the waterplane in a

hydrostatic state along the centerline in the moving direction: one positioned midway between the two ships and the others at the bow of the follower and stern of the leader, as shown in Figure 20.

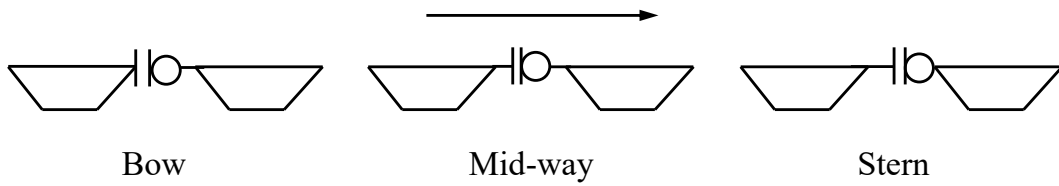


Figure 20. Three installation positions of joints.

Figure 21 illustrates the heave motion for these different joint positions between the ships. Notably, there is no difference in the heave and pitch motions among three installation positions. This is because the sliding-hinged connection allows for the release of heave and pitch motions, with no moment or vertical force acting on the joint in head sea. Additionally, surge motion remains unaffected by horizontal shifts of the joint along the x-axis.

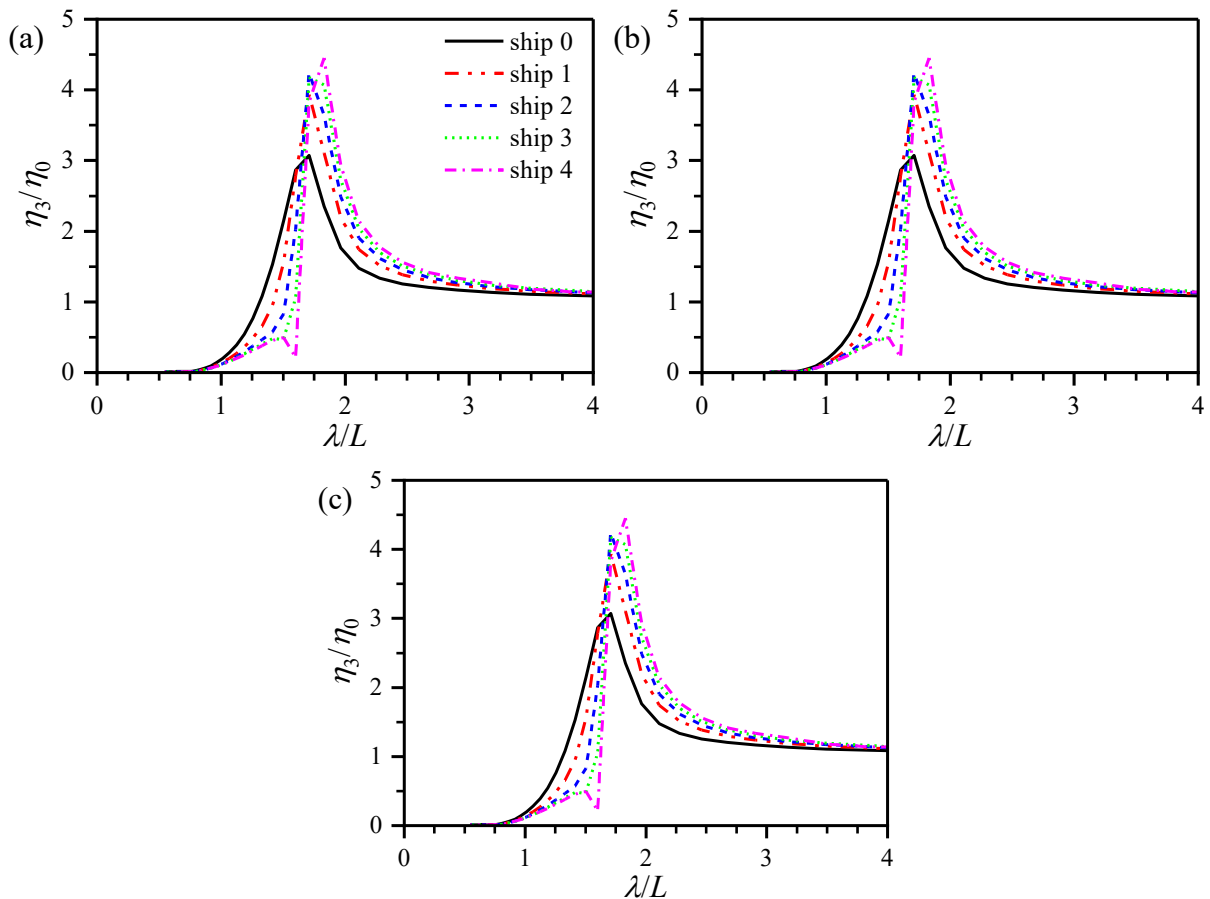


Figure 21. Heave motion for different positions of joints with a gap of $0.1 L$ at $F_r = 0.3$. (a) Bow; (b) Midway.

5.3 Effect of gaps between two ships

The spacing between two ships plays a crucial role in ensuring safe operations in waves,

particularly in preventing collisions. The gap between two ships may influence their motion responses by wave superposition or cancellation. Figure 22 illustrates the heave motions for these varying gaps. The results indicate that the motion responses of these ships exhibit minimal variation across gaps $0.1L$ to $0.4L$. It is attributed to the relatively small difference in gap size compared to the wavelength. When designing a marine train with barges connected by joints, the gap between two ships should remain relatively small from an engineering perspective. As a result, the effect of gaps on ship motions is generally minimal, except in conditions with very short wavelengths, where the gap may have a more significant impact.

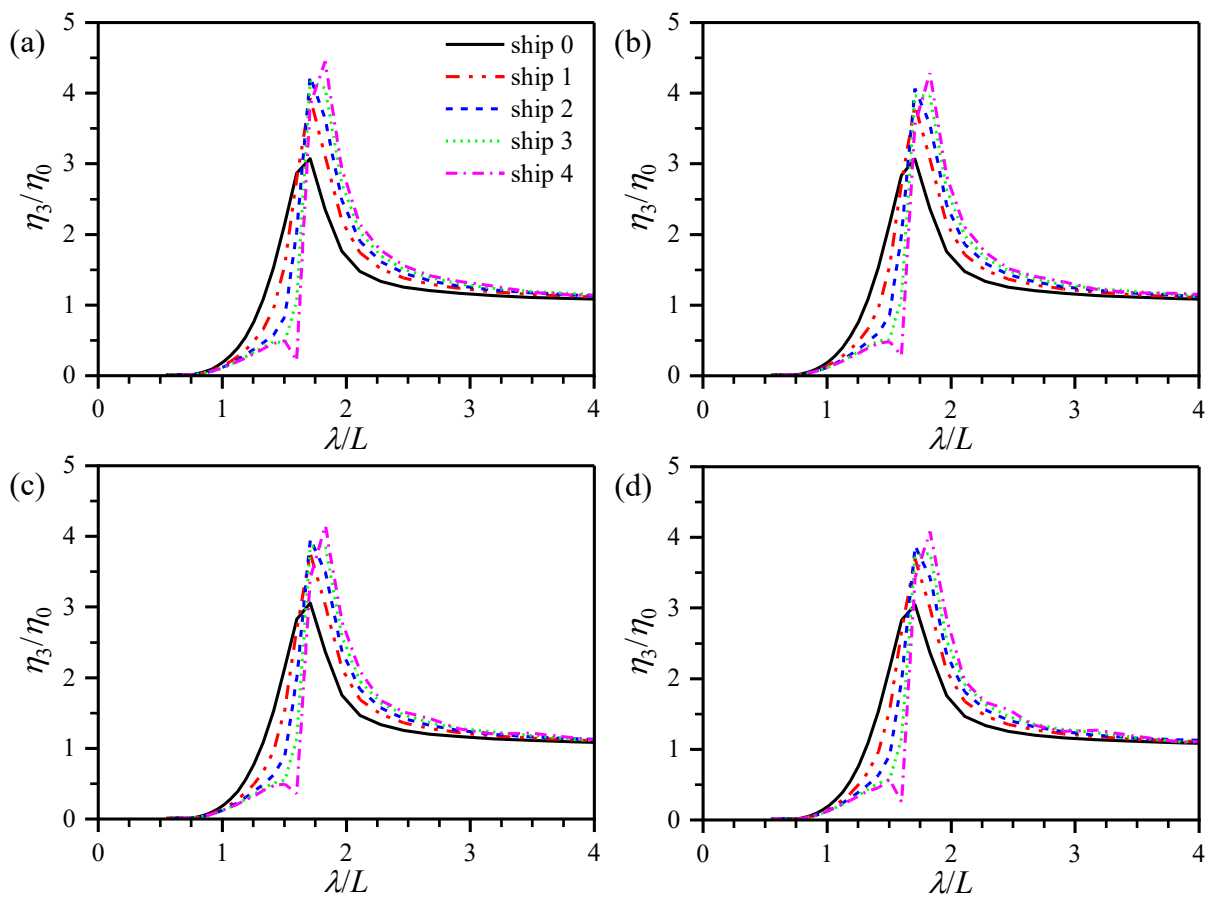


Figure 22. Heave motion at different gaps between two ships at $F_r = 0.3$. (a) $0.1L$; (b) $0.2L$; (c) $0.3L$; (d) $0.4L$.

6. Conclusions

This study analyzed the hydrodynamic responses of marine trains, a system of multiple ships advancing in a row, by considering the effect of hydrodynamic interactions and mechanical connection. The numerical approach was validated against the published experimental and numerical data, showing strong agreement with previously published data. Using the validated in-house code MHydro, the

hydrodynamic responses of various marine train configurations were examined, focusing on the effects of physical parameters such as non-physical and physical connections, moving speed, joint installation positions, and gaps between ships. The key findings of the numerical analyses are summarized as follows:

- (1) When a marine train system without physical connection advances in a head sea, the RAOs of the leading ship remain consistent with those of a single ship at the same speed, particularly at higher speeds, as the waves generated by the trailing ship have minimal impact on the wave field encountered by the leading ship. In contrast, the RAOs of the trailing ship are notably influenced by the waves generated by the leading ship.
- (2) When adjacent ships are either hinged or rigidly connected, their motion RAOs are significantly lower than those of free ships. However, these two connection types experience considerable vertical shear forces at the joints, which may lead to potential joint damage. In contrast, the use of sliding-hinged joints maintains motion responses without increasing them, while greatly reducing vertical shear forces and diminishing the risk of joint failure, providing a suitable choice for the connection form of marine trains in practical engineering applications.
- (3) In head sea conditions, the motion RAOs for ships with sliding-hinged connections are identical to those observed with non-physical connections. However, in oblique sea conditions, the roll motion differs significantly between the two connection types, as sliding-hinged connections restrict relative roll motion between the vessels.
- (4) As the advancing speed increases, the motion RAOs of the ships in a marine train system with sliding-hinged joints increase significantly, particularly near the resonance zone. To ensure operational safety in engineering practice, a maximum allowable speed should be specified. In contrast, the installation position of the joints and the gap between ships have minimal impact on their motion responses within the marine train configuration, thereby saving time spent on optimizing these two parameters during the design phase.

Overall, this study provides some insights into enhancing the design of marine trains, to ensure the long-term sustainability and reliability of marine transport systems. It should be noted that viscous

damping is not considered in the numerical simulation, which may lead to high motion response amplitudes, especially near resonance. Future CFD simulations or physical experiments should be conducted to obtain accurate viscous damping coefficients.

Acknowledgements

Results were obtained using the ARCHIE-WeSt High Performance Computer (www.archie-west.ac.uk) based at the University of Strathclyde.

Author Contributions

Feng-Shen Zhu: Conceptualization, Methodology, Investigation, Writing - original draft. **Zhi-Ming Yuan:** Conceptualization, Methodology, Investigation, Supervision, Writing – review & editing. **De-Feng Wu:** Conceptualization, Investigation, Writing – review & editing. **De-Qing Zhang:** Conceptualization, Methodology, Investigation, Writing – review & editing.

Data availability statement

The data that support the findings of this study are available from the corresponding author upon reasonable request.

References

- Anderson, E.M., 2013. Seasnake: A versatile concept, https://www.porttechnology.org/technical-papers/seasnake_a_versatile_concept/.
- Bispo, I., Mohapatra, S., Soares, C.G., 2022. Numerical analysis of a moored very large floating structure composed by a set of hinged plates. *Ocean Engineering* 253, 110785.
- Brown, R., Runyon, N., 2022. A Study of Energy Efficiency in Articulating Tug and Barge Design. Doctors, L.J., Beck, R.F., 1987. Numerical aspects of the Neumann-Kelvin problem. *Journal of ship Research* 31 (01), 1-13.
- DPRPA, 2020. Sea Train Contract Opportunity Notification of the US Defense Advanced Research Projects Agency. <https://sam.gov/opp/e12d9874440945dcb2d78709d2361c30/view#general>.
- Gao, R., Tay, Z., Wang, C., Koh, C., 2011. Hydroelastic response of very large floating structure with a flexible line connection. *Ocean Engineering* 38 (17-18), 1957-1966.
- Guha, A., Somayajula, A., Falzarano, J., 2013. Analysis of causeway ferry dynamics for safe operation of improved navy lighterage system, *Proceedings of the 13th International Ship Stability Workshop*, pp. 1-8.

- Hess, J.L., Smith, A.M.O., 1964. Calculation of nonlifting potential flow about arbitrary three-dimensional bodies. *Journal of ship research* 8 (04), 22-44.
- Journee, J., 1992. Experiments and calculations on four Wigley hull forms.
- Karafiath, G., Metcalf, B., Geisbert, J., 2009. Seatrain for High-Capacity High-Speed Ocean Transport, *Proceedings of FAST 2009, International Conference on Fast Sea Transportation*.
- Li, Z., Chen, D., Feng, X., 2023. Hydroelastic and expansibility analysis of a modular floating photovoltaic system with multi-directional hinge connections. *Ocean Engineering* 289, 116218.
- Miller, A., Barbosa, J., Latorre, R., 2001. Analysis of tug-barge connection force measurements. *Marine technology and SNAME news* 38 (02), 130-137.
- Mizine, I., Karafiath, G., 2015. Model Test Evaluation of High Speed Trimaran (HST) Sea Train Concept, *SNAME International Conference on Fast Sea Transportation*. SNAME, p. D011S003R004.
- Mumford, D.K., 1993. Vertical forces on the coupling of a pusher tug-barge. University of British Columbia.
- Newman, J.N., 1994. Wave effects on deformable bodies. *Applied ocean research* 16 (1), 47-59.
- Qin, Y., Wang, Q., Dong, G., Yao, C., Feng, D., 2023. Hydrodynamic Performance of a Conceptional Seatrain in Heading Wave Based on Small Water Plane Area Trimaran, *International Conference on Offshore Mechanics and Arctic Engineering*. American Society of Mechanical Engineers, p. V005T006A082.
- Ren, N., Zhang, C., Magee, A.R., Hellan, Ø., Dai, J., Ang, K.K., 2019. Hydrodynamic analysis of a modular multi-purpose floating structure system with different outermost connector types. *Ocean Engineering* 176, 158-168.
- Ronæss, M., 2002. Wave induced motions of two ships advancing on parallel course (Ph.D thesis). NTNU, Norway.
- Shabana, A.A., 2009. *Computational dynamics*. John Wiley & Sons.
- Sun, L., Taylor, R.E., Choo, Y.S., 2011. Responses of interconnected floating bodies. *The IES Journal Part A: Civil & Structural Engineering* 4 (3), 143-156.
- Vinogradov, A.M., Krasil'shchik, I.S., 1975. What is the Hamiltonian formalism? *Russian mathematical surveys* 30 (1), 177.
- Wadam, D., 2010. *Wave analysis by diffraction and Morison theory*. SESAM user manual. Det Norske Veritas, Høvik.
- Yuan, Z.-M., Chen, M., Jia, L., Ji, C., Incecik, A., 2021. Wave-riding and wave-passing by ducklings in formation swimming. *Journal of Fluid Mechanics* 928, R2.
- Yuan, Z.-M., Incecik, A., Dai, S., Alexander, D., Ji, C.-Y., Zhang, X., 2015. Hydrodynamic interactions between two ships travelling or stationary in shallow waters. *Ocean Engineering* 108, 620-635.
- Zhang, D., Du, J., Yuan, Z., Yu, S., Li, H., 2023. Motion characteristics of large arrays of modularized floating bodies with hinge connections. *Physics of Fluids* 35 (7).
- Zhang, L., Xing, L., Dong, M., Chen, W., 2021. Resistance Tests of an Articulated Pusher Barge System in Deep and Shallow Water, *International Conference on Offshore Mechanics and Arctic Engineering*. American Society of Mechanical Engineers, p. V006T006A035.
- Zhu, F., Yuan, Z.-m., 2024. Wave drag and wave patterns by ships moving in a single-file formation. *Physics of Fluids* 36 (6).